

## Physics and optimization of plasma startup in the RFP

This content has been downloaded from IOPscience. Please scroll down to see the full text.

2015 Nucl. Fusion 55 053004

(<http://iopscience.iop.org/0029-5515/55/5/053004>)

View [the table of contents for this issue](#), or go to the [journal homepage](#) for more

Download details:

IP Address: 128.104.165.161

This content was downloaded on 15/07/2015 at 18:40

Please note that [terms and conditions apply](#).

# Physics and optimization of plasma startup in the RFP

W. Mao<sup>1</sup>, B.E. Chapman<sup>2</sup>, W.X. Ding<sup>3,1</sup>, L. Lin<sup>3</sup>, A.F. Almagri<sup>2</sup>,  
J.K. Anderson<sup>2</sup>, D.J. Den Hartog<sup>2</sup>, J. Duff<sup>2</sup>, J. Ko<sup>2</sup>,  
S.T.A. Kumar<sup>2</sup>, L. Morton<sup>2</sup>, S. Munaretto<sup>2</sup>, E. Parke<sup>2</sup>,  
J.A. Reusch<sup>2</sup>, J.S. Sarff<sup>2</sup>, J. Waksman<sup>2</sup>, D.L. Brower<sup>3</sup> and W. Liu<sup>1</sup>

<sup>1</sup> CAS Key Laboratory of Basic Plasma Physics and Department of Modern Physics, University of Science and Technology of China, Hefei 230026, People's Republic of China

<sup>2</sup> Department of Physics, University of Wisconsin, Madison, WI 53706, USA

<sup>3</sup> Department of Physics and Astronomy, University of California, Los Angeles, CA 90095, USA

E-mail: [maozhe@mail.ustc.edu.cn](mailto:maozhe@mail.ustc.edu.cn)

Received 28 September 2014, revised 6 February 2015

Accepted for publication 5 March 2015

Published 9 April 2015



CrossMark

## Abstract

In the tokamak and reversed-field pinch (RFP), inductively driven toroidal plasma current provides the confining poloidal magnetic field and ohmic heating power, but the magnitude and/or duration of this current is limited by the available flux swing in the poloidal field transformer. A portion of this flux is consumed during startup as the current is initiated and ramped to its final target value, and considerable effort has been devoted to understanding startup and minimizing the amount of flux consumed. Flux consumption can be reduced during startup in the RFP by increasing the toroidal magnetic field,  $B_{ti}$ , applied to initiate the discharge, but the underlying physics is not yet entirely understood. Toward increasing this understanding, we have for the first time in the RFP employed advanced, non-invasive diagnostics on the Madison Symmetric Torus to measure the evolution of current, magnetic field, and kinetic profiles during startup. Flux consumption during startup is dominantly inductive, but we find that the inductive flux consumption drops as  $B_{ti}$  increases. The resistive consumption of flux, while relatively small, apparently increases with  $B_{ti}$  due to a smaller electron temperature. However, the ion temperature increases with  $B_{ti}$ , exceeding the electron temperature and thus reflecting non-collisional heating. Magnetic fluctuations also increase with  $B_{ti}$ , corresponding primarily to low- $n$  modes that emerge sequentially as the safety factor profile evolves from tokamak-like to that of the RFP.

Keywords: reversed-field pinch, start up, flux consumption, magnetic field profile

(Some figures may appear in colour only in the online journal)

## 1. Introduction

In the tokamak and reversed-field pinch (RFP), inductively driven toroidal plasma current provides the poloidal magnetic field and ohmic plasma heating. Subject to stability and other limits, it is often desirable to drive the maximum possible toroidal current for the maximum possible time. But the magnitude and/or duration of this current is limited by the available flux swing in the poloidal field transformer. This is a particularly stringent limit in the spherical (very-low-aspect-ratio) tokamak [1] given the necessarily small central hole in the device which places a severe limit on the available flux swing. This is also a stringent limit in the RFP given this configuration's larger loop voltage and consequently larger resistive consumption of transformer flux. A substantial fraction of the available flux is consumed during startup, the time during which the toroidal current is initiated and ramped to its final target value. Considerable effort has

been devoted to understanding and optimizing startup in the tokamak, and methods including coaxial and point source helicity injection have been developed for minimizing the consumption of transformer flux, e.g. [2–6]. Effort has been devoted to understanding and optimizing startup in the RFP as well, e.g. [7–10]. It has long been known in the RFP that poloidal field transformer flux consumption during startup can be reduced by increasing the initial toroidal magnetic field. But the underlying physics of this observation, and of startup in general, is not yet entirely understood.

Toward increasing this understanding, we have for the first time in the RFP employed advanced, non-invasive diagnostics on the Madison Symmetric Torus (MST) [11] to measure the evolution of the internal current, magnetic field, and kinetic profiles during startup. We compare the evolution of these profiles and related quantities with different values of the initial toroidal magnetic field,  $B_{ti}$ . As in other RFP's, poloidal field transformer flux consumption drops during startup as  $B_{ti}$

is increased. Efficient utilization of transformer flux is of particular importance for the MST, since the MST's poloidal field system is based on primary windings wrapped around a 2 Wb iron core, and this flux swing presently limits the peak current and the time over which this current can be sustained.

From our measurements, transformer flux consumption during startup is dominantly inductive, not resistive, and we find that a drop in the inductive flux consumption occurs with an increase in  $B_{ti}$ . While relatively small regardless of  $B_{ti}$ , resistive flux consumption apparently increases with  $B_{ti}$ . This is due to a smaller electron temperature that occurs despite the fact that the toroidal (ohmic) current is larger with larger  $B_{ti}$ . On the other hand, the ion temperature increases with  $B_{ti}$  and is larger than the electron temperature, reflecting non-collisional ion heating. These differences in electron and ion temperature are accompanied by larger and longer sustained low- $n$ ,  $m = 1$  magnetic fluctuations that emerge sequentially as the safety factor profile evolves from a tokamak-like shape to the final RFP equilibrium.

The structure of this paper is as follows. The temporal evolution of basic equilibrium parameters with different  $B_{ti}$  is compared first. Following this, we compare the evolution of the magnetic field and current density profiles. We then present the evolution of the safety factor profile and discuss the relationship with the measured MHD activity. We then examine the evolution of the density and temperature, and we estimate beta and the energy confinement time. Finally, we discuss the inductive and resistive consumption of flux.

## 2. Basic equilibrium parameters

One of the primary goals of this paper is the diagnosis and comparison of the temporal evolution of plasma parameters with different values of  $B_{ti}$ , applied for the initiation of each discharge. Some of the key parameters are shown in figure 1, which displays data from MST discharges with different  $B_{ti}$ . In terms of external control, the only difference between these discharges is in  $B_{ti}$ , as shown at time  $t = 0$  ms in figure 1(b). The toroidal plasma current,  $I_p$ , ramps up at different rates in each discharge but reaches the same final value, 600 kA, at about the same time. This is about the largest  $I_p$  of which MST is presently capable. The average toroidal field (toroidal flux) in the plasma ramps up with  $I_p$ . This is given the fact that poloidal plasma current ramps up with the toroidal plasma current. While the average  $B_t$  grows, the value at the plasma boundary decreases and eventually reaches zero. This is reflected in the toroidal field reversal parameter,  $F \equiv B_t(a)/\langle B_t \rangle$ . The mode of startup utilized here is termed self-reversal [12], wherein the increase in the toroidal flux embedding the plasma induces a steady decrease in the toroidal field at the boundary. However, to simplify the comparison between these four cases, current in the toroidal field circuit is largely suppressed, but not altogether eliminated, when  $B_t(a)$  reaches zero, thereby maintaining  $B_t(a) \sim 0$ . As is observed in figure 1(c), the time for  $F$ , and  $B_t(a)$ , to reach zero increases as  $B_{ti}$  increases. Self-reversal sets a practical upper bound on  $B_{ti}$ . Above the largest  $B_{ti}$  used here,  $B_t(a)$  cannot reach zero, and the discharge terminates prematurely. The toroidal electric field responsible for  $I_p$  is induced by a flux change in MST's iron-core transformer. The flux evolution in the transformer is

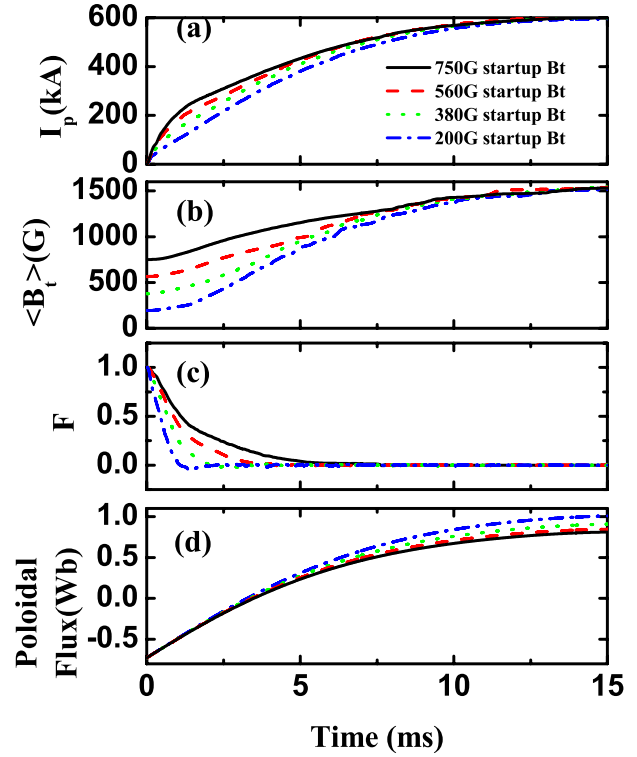


**Figure 1.** With four different values of  $B_{ti}$ , temporal waveforms of (a) toroidal plasma current, (b) cross-section-averaged toroidal magnetic field, (c) reversal parameter, defined in the text, and (d) poloidal transformer flux. Each waveform is based on an ensemble average of similar discharges.

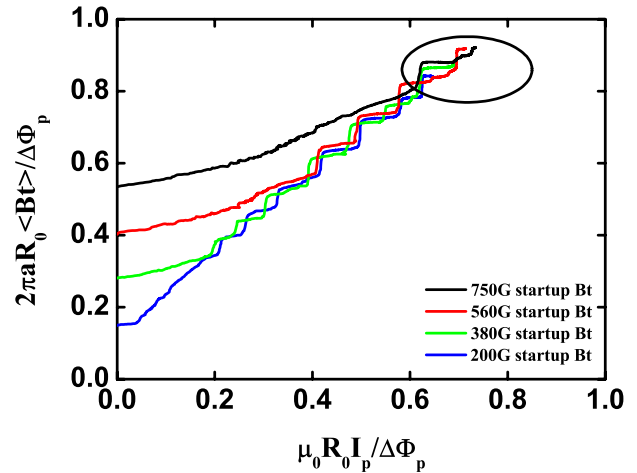


**Figure 2.** Trajectories through  $\langle B_t \rangle - I_p$  space for four different  $B_{ti}$  cases. Both  $\langle B_t \rangle$  and  $I_p$  have been normalized by poloidal flux swing  $\Delta\Phi_p$ . The oval in the plot highlights the positions of the trajectories after startup is complete. The same maximum  $I_p$  is reached in all four cases but with a different  $\Delta\Phi_p$ . Hence, the above trajectories terminate more and more to the right as  $B_{ti}$  increases.

shown in figure 1(d). As the initial toroidal field is increased, the flux consumed during startup is decreased.

To make the relation between  $B_{ti}$  and maximum  $I_p$  more clear, we show in figure 2 the RFP mode startup trajectories through  $\langle B_t \rangle - I_p$  space in four different  $B_{ti}$  cases. The variables plotted here are the same as in figure 9 of [12]. The four startup trajectories in this plot are quite disparate initially but converge

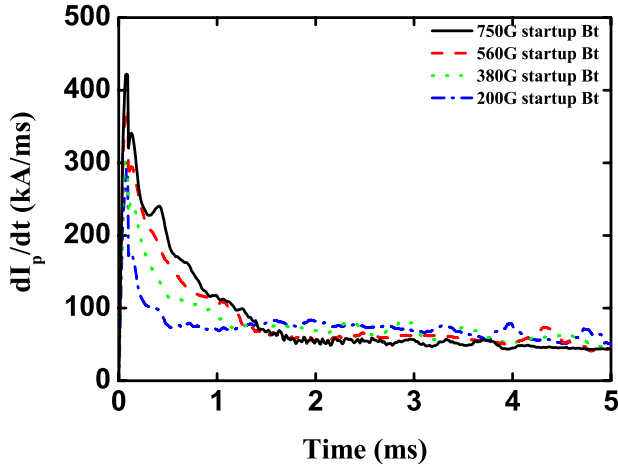


**Figure 3.** Rate of increase of toroidal plasma current for different  $B_{ti}$ . Each waveform is based on an ensemble average of similar discharges.

as  $I_p$  ramps up. As expected from the data in figure 1, the final value of  $I_p$ , normalized to the poloidal flux swing in the transformer, grows with  $B_{ti}$ .

It is clear from figure 1(a) that the initial toroidal plasma current ramps up more and more rapidly as  $B_{ti}$  is increased. This is shown in detail in figure 3. These differing initial ramp rates occur in spite of the fact that the applied toroidal voltage is about the same in each case. After 1.5 ms, however, the initially fast ramp for the highest  $B_{ti}$  case transitions to a slower ramp. This evolution is likely due to the differences, described later, in the internal inductance and resistance that accompany the different values of  $B_{ti}$ . Figure 4 shows in more detail how  $I_p$  responds to the driving voltage as the equilibrium evolves.  $V_{tor}(a)$  is the surface toroidal voltage. The ratio of the current derivative to the applied voltage is plotted versus  $F$ , which partly represents the magnetic equilibrium and which evolves with time from right to left. This is indicated by arrows in each plot. For a given  $V_{tor}(a)$  and  $F$ ,  $I_p$  clearly rises more rapidly with larger  $B_{ti}$ . To close out this section, the poloidal transformer flux expended during startup for each of the four cases is shown in figure 5. The consumed flux drops by 0.2 Wb over the range of  $B_{ti}$  applied here. This is 10% of the total available flux swing.

### 3. Profiles of magnetic field and current density

To begin to understand the physics underlying the data shown above, we show in this section the temporal evolution of the internal magnetic field and current density profiles. Profiles of the toroidal current density,  $J_t$ , and poloidal magnetic field,  $B_p$ , are measured by an 11-chord far-infrared (FIR) laser polarimeter–interferometer, which also provides the electron density profile [13]. Via Faraday rotation, polarimetry measures the line-integral of the product of the electron density and magnetic field along each laser chord, and the simultaneous but separate measurement of the electron density allows one to extract the magnetic field. Profiles of the poloidal current density,  $J_p$ , and toroidal magnetic field,  $B_t$ , are obtained from equilibrium reconstruction constrained by the FIR and other data. The reconstruction code employed here is FIRfit [14].

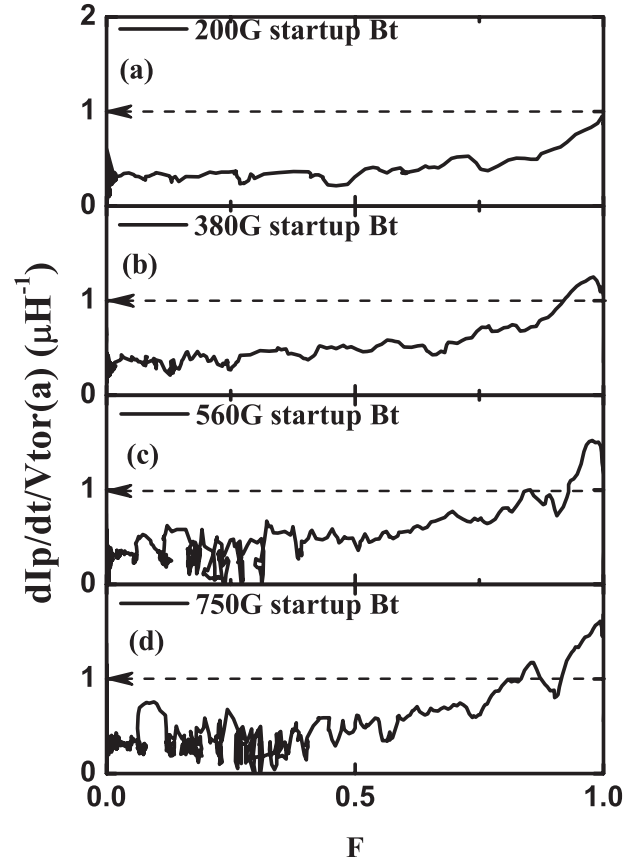


**Figure 4.** Ratio of the plasma current time derivative to the surface toroidal voltage for different  $B_{ti}$  versus the reversal parameter. The reversal parameter evolves in time from right to left and is partially representative of the magnetic equilibrium.

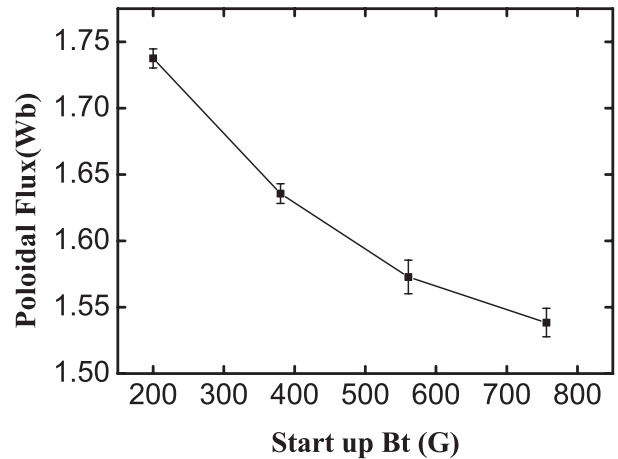


**Figure 5.** Poloidal core flux consumption for different  $B_{ti}$ . Each point is based on an ensemble average of similar discharges.

Ampere's law,  $\nabla \times \mathbf{B} = \mu_0 \mathbf{J}$ , and the definition,  $\lambda \equiv \mu_0 a J_{par}/B$ , are applied in a cylindrical coordinate system resulting in

$$\frac{dB_t}{dr} = -\frac{\lambda}{a} \frac{B_t^2 + B_p^2}{B_p} + B_t \left( \frac{1}{r} + \frac{1}{B_p} \frac{dB_p}{dr} \right).$$

From the measured  $B_p$  profile, the above equation is solved numerically to obtain the profile of  $B_t$ . The profile of  $\lambda$

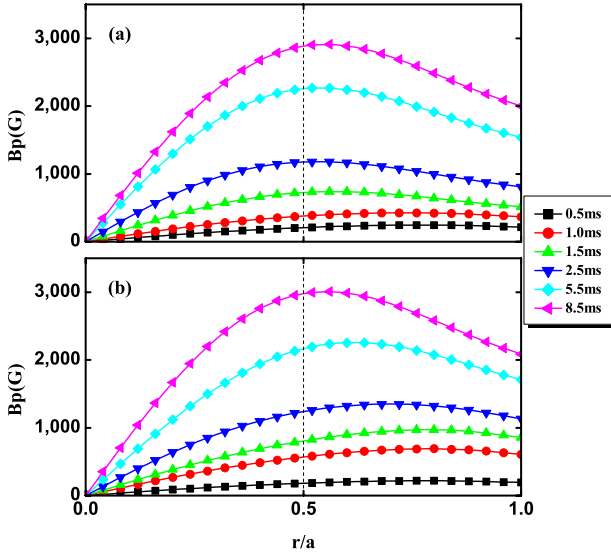


**Figure 6.** Temporal evolution of poloidal magnetic field profiles during startup for (a) low  $B_{ii} = 200$  G (shot 1121002097), (b) high  $B_{ii} = 750$  G (shot 1121002015).

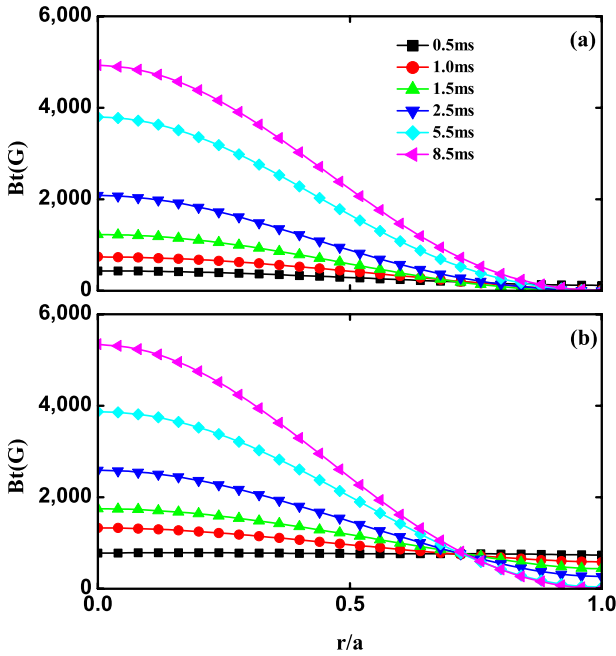


**Figure 7.** Temporal evolution of toroidal magnetic field profiles during startup for the same (a) low- $B_{ii}$  and (b) high- $B_{ii}$  shots as in figure 6. Origin of inflection point in (b) is not yet understood.

is specified as  $\lambda(r) = \lambda_0(1 - (r/a)^\alpha)$ , and the two free parameters ( $\lambda_0$  and  $\alpha$ ) are determined iteratively in the solution of the above equation by adding two additional measured constraints,  $B_t(a)$  and the cross-section-averaged value of  $B_t$ . Toroidal effects are included by using the shifted circular flux surface approximation.

From the discharges with the largest (750 G) and smallest (200 G)  $B_{ii}$ , the magnetic field profiles are shown in figures 6 and 7, and the current density profiles are shown in figures 8 and 9. The earliest profile in each plot is at 0.5 ms, which is the earliest time that data from the polarimeter is useful. Comparing the evolution of  $B_p$  between the two cases, figure 6,

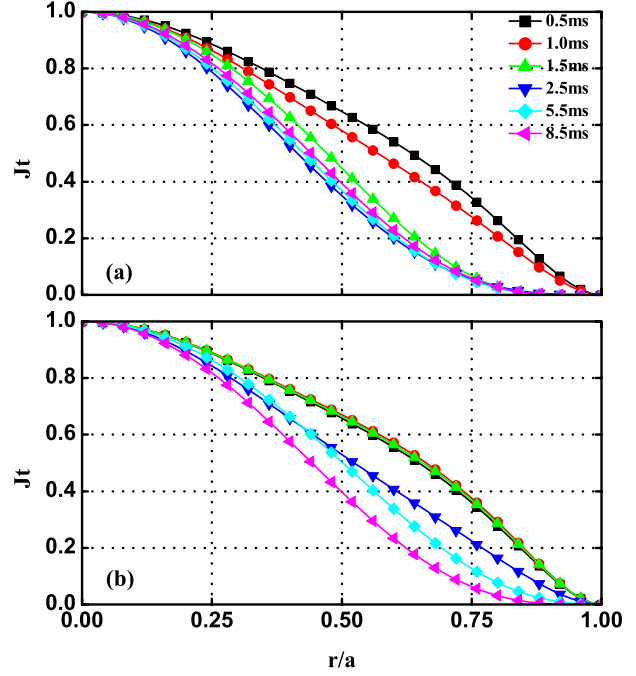


**Figure 8.** Temporal evolution of toroidal current density profiles during startup for the same (a) low- $B_{ii}$  and (b) high- $B_{ii}$  shots as in figure 6. Each profile is normalized to its central value.

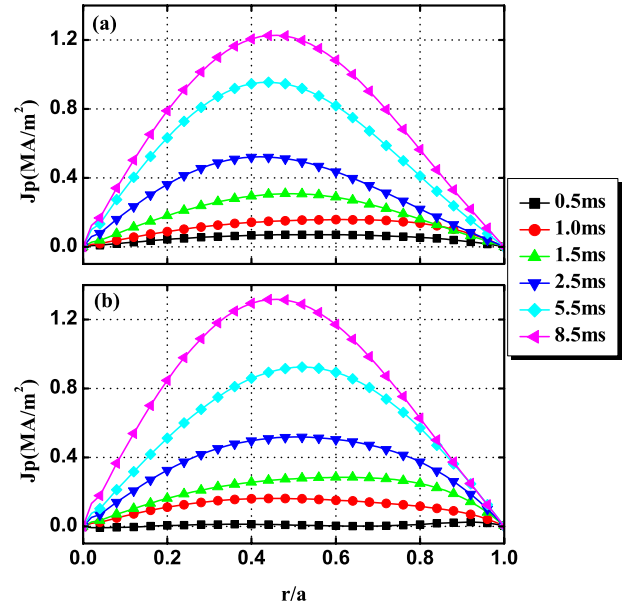


**Figure 9.** Temporal evolution of poloidal current density profiles during startup for the same (a) low- $B_{ii}$  and (b) high- $B_{ii}$  shots as in figure 6.

the maximum in each profile from 0.5–5.5 ms occurs at larger radius in the case with larger  $B_{ii}$ . This corresponds to a broader profile of  $J_t$ , as shown in figure 8, implying a smaller toroidal inductance, described later. The temporal evolution of the  $B_t$  profiles is shown in figure 7. As expected,  $B_t$  is initially larger everywhere with larger  $B_{ii}$ , and more time is required for  $B_t(a)$  to reach zero. The poloidal current density evolution is shown in figure 9. Similar to the toroidal current density profiles, the poloidal current density generally peaks at larger radius with higher  $B_{ii}$ .

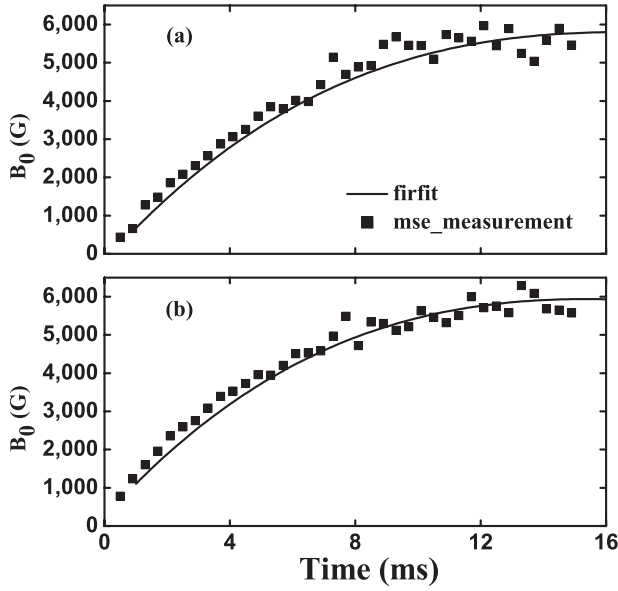


**Figure 10.** Comparison of central  $B_t$  from FIRfit with MSE data for the same (a) low- $B_{ti}$  and (b) high- $B_{ti}$  shots as in figure 6.

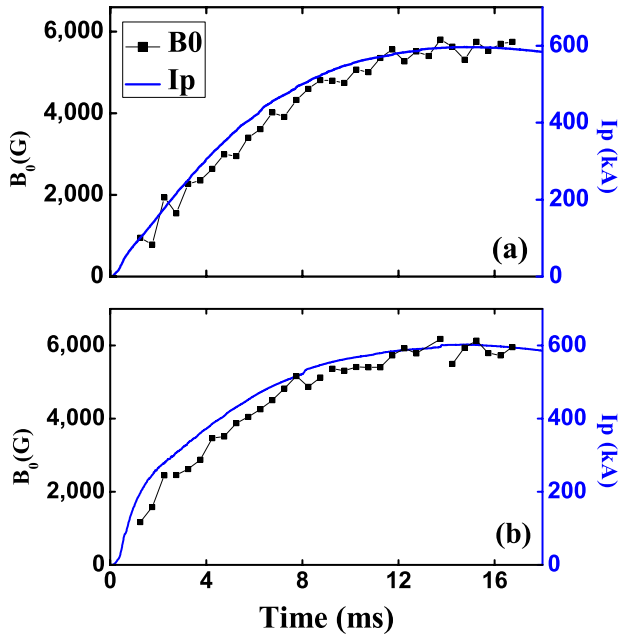


**Figure 11.** Evolution of central  $B_t$  measured with MSE and toroidal plasma current for the same (a) low- $B_{ti}$  and (b) high- $B_{ti}$  shots as in figure 6.

As one check of these reconstructions, we compare the FIRfit-reconstructed evolution of  $B_0$ , the on-axis value of  $B = B_t$ , to that measured directly with a motional Stark effect diagnostic (MSE) [15]. Two such comparisons are shown in figure 10. The FIRfit data agree well with the directly measured value for both low and high  $B_{ti}$ . This helps establish that FIRfit is suitable for analysing the MST equilibrium during startup, something which had not been attempted previously.

In figure 11 we overlay the MSE data points and the  $I_p$  waveform. Since under most conditions, the source of toroidal flux in the plasma is largely the applied poloidal flux, one expects  $B_0$  to scale linearly with  $I_p$ , and this has been confirmed

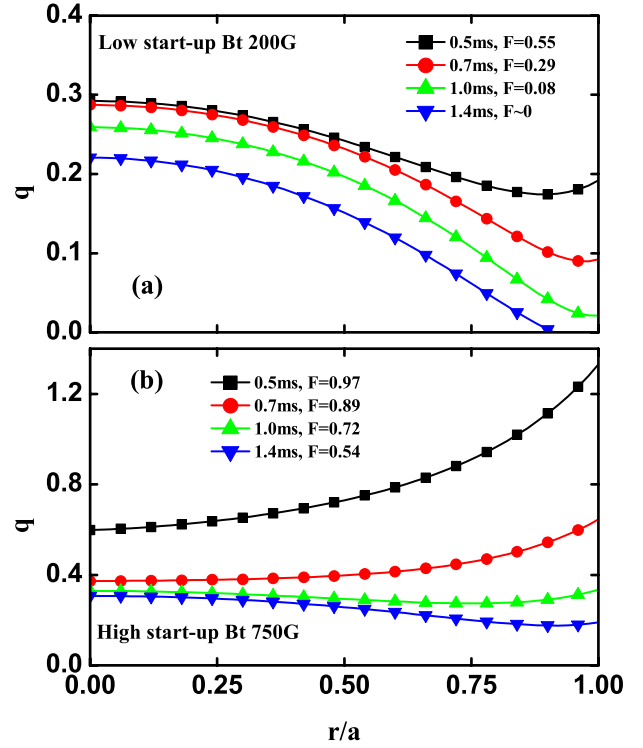


**Figure 12.** Evolution of safety factor profiles very early in startup for the same (a) low- $B_{ti}$  and (b) high- $B_{ti}$  shots as in figure 6. The values of the reversal parameter are indicated at each time point.

in the  $I_p$  flattop phase of MST plasmas [14]. With the MSE data in figure 11 adjusted to align with  $I_p$  at the end of the time window,  $B_0$  tracks  $I_p$  reasonably well over the entire time window for the low- $B_{ti}$  shot, but for high  $B_{ti}$ , the two parameters deviate from one another to a larger extent early in time. This is consistent with the fact that a substantial fraction of the initial toroidal flux in the high- $B_{ti}$  case is provided by the toroidal field circuit.

#### 4. Safety factor evolution and magnetic fluctuations

In this section we describe the evolution of the safety factor profile and associated MHD activity during startup. This reveals some important differences in the evolution of discharges with different  $B_{ti}$ , and it serves as a further check of the equilibrium reconstructions. The safety factor,  $q = (r/R)(B_t/B_p)$ , is computed with FIRfit. The evolution of the  $q$  profiles very early in time is shown in figure 12 for the discharges described in the previous section. In the discharge with low  $B_{ti}$ , the  $q$  profile very rapidly evolves to a shape characteristic of the RFP where  $q$  decreases from the core to the edge and is everywhere less than 1. Note that  $Bt(a)$  reaches zero at about 1.3 ms. Due to discrete magnetic reconnection events occurring after that time, small bursts of current are induced in the external toroidal field circuit, and  $Bt(a)$  drops momentarily below zero. This is reflected in  $q(a)$  at 1.4 ms. In the discharge with high  $B_{ti}$ ,  $q$  initially increases from the core to the edge with a value  $> 1$  at the boundary. This is similar in shape to a tokamak equilibrium.

The  $q$  profile evolution later in startup is shown in figure 13. In the low- $B_{ti}$  case, in spite of the fact that  $I_p$  is

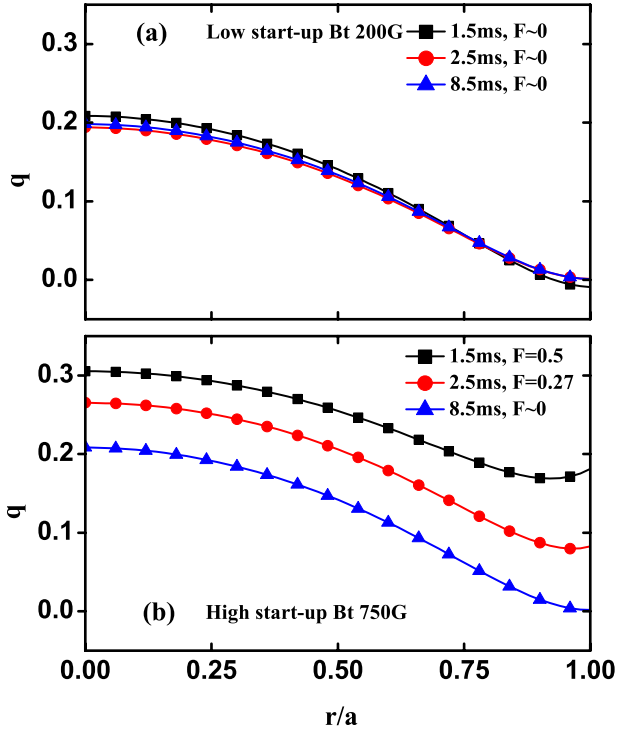


**Figure 13.** Evolution of safety factor profiles later in startup for the same (a) low- $B_{ti}$  and (b) high- $B_{ti}$  shots as in figure 6. The values of the reversal parameter are indicated at each time point.

ramping up strongly during this time,  $q(r) \sim \text{constant}$ . Both the poloidal and toroidal fields are generated entirely by plasma current during this time. On the other hand,  $q(r)$  continues to evolve in the high- $B_{ti}$  case, due in part to the fact that substantial current is still flowing in the toroidal field circuit. But late in the time window shown here, after  $B_t(a)$  reaches zero, the profile assumes the same shape and magnitude as the low- $B_{ti}$  profile.

The safety factor profiles shown above provide a number of low-order rational surfaces which can play host to  $m \geq 1$  instabilities that cause substantial fluctuations in the magnetic field. Moreover, the local minima appearing near the edge lead to the same resonant value of  $q$  appearing at two locations in the plasma. This can lead to the emergence of ideal instabilities [16, 17]. Shown in figure 14(a) is the rms amplitude of the largest fluctuations in each of the four  $B_{ti}$  cases. These fluctuations, measured with a toroidal array of magnetic sensing coils at the plasma boundary, have poloidal mode number  $m = 1$  and toroidal mode numbers  $n = 1 - 9$ . In the first few ms in figure 14, the fluctuations initially rise but then fall to the final minimum saturated value which in each case is reached around the time that  $q(a)$  reaches zero. As shown in figure 14(b), which contains the fluctuation amplitudes normalized to  $B_p(a)$ , the fluctuation level is around 1% after startup, but it ranges as high as 6–8% during startup. The waveforms in figure 14(b) differ from those in figure 14(a) due to the different ramp rates in  $I_p$  and  $B_p(a)$ , but the fluctuation amplitude in both plots is sustained at an enhanced value for the longest time in the highest- $B_{ti}$  discharge.

For the highest and lowest  $B_{ti}$  cases, figure 15 displays the evolution of the individual modes comprising the rms data in figure 14. In the highest  $B_{ti}$  case, the  $n = 1$  to  $n = 4$  modes

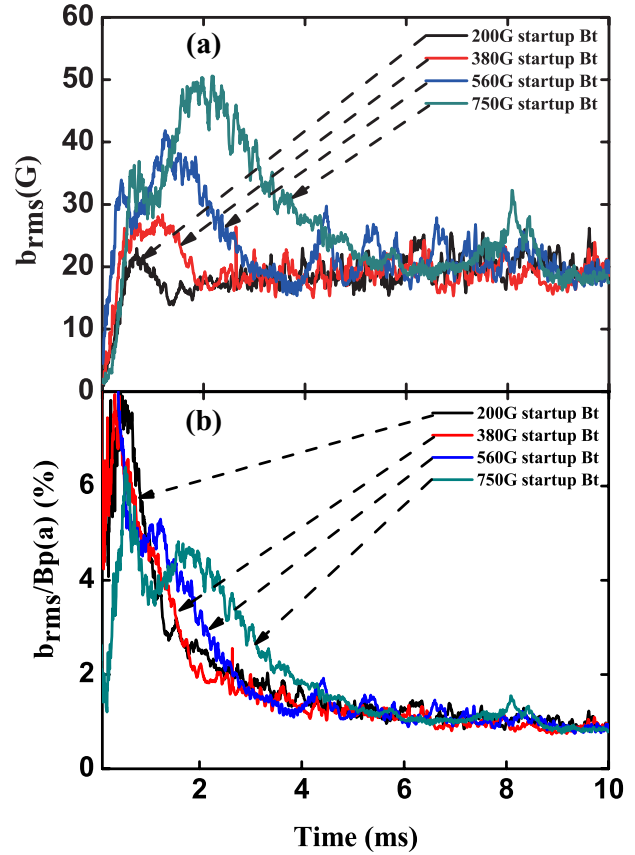


**Figure 14.** (a) Root mean square of poloidal fluctuation amplitudes and (b) fluctuation amplitudes normalized to the poloidal magnetic field at the plasma boundary for  $n = 1 - 9$  for the four discharges with different  $B_{ti}$ . The shot numbers are 1121002015, 1121002042, 1121002071, 1121002096 from high  $B_{ti}$  to low  $B_{ti}$ .

rise and fall successively, reflecting in part the evolution of the associated resonant surfaces with  $q = m/n = 1/1, 1/2, 1/3$  and  $1/4$ . These surfaces appear and subsequently disappear as  $q(r)$  evolves. By the time  $q(a)$  reaches zero, these lowest  $n$  mode amplitudes are very small, near the noise level of the measurement. The  $n = 5 - 8$  modes in figure 15(b) exhibit the same initial rise and fall as the  $n = 1 - 4$ , but since their resonant surfaces remain in the plasma after  $q(a)$  reaches 0, their amplitudes remain finite. In sharp contrast, in the lowest  $B_{ti}$  case the  $q$  profile evolves so quickly to its final state that one cannot distinguish the evolution of the various modes, and the peak amplitude of each mode is generally smaller than its counterpart with high  $B_{ti}$ . The final saturated amplitudes of the  $n = 5 - 8$  are, however, comparable between the two cases, as expected. These final amplitudes, coupled with the relatively close spacing of adjacent rational surfaces, are sufficient to stochasticize the magnetic field in the plasma core [18, 19]. Given the larger mode amplitudes early in the high- $B_{ti}$  discharge, the magnetic field may be stochastic here as well. Note that the sequential rise and fall of the low- $n$ ,  $m = 1$  modes was also observed in the RFX-mod RFP, for one value of  $B_{ti}$  [8]. MHD stability analysis of the RFX-mod data confirmed that the various  $m = 1$  modes are born as linear ideal instabilities following the appearance of their respective resonant surfaces in the plasma.

The initial difference in fluctuation amplitudes shown above is with respect to specific modes with toroidal rotation

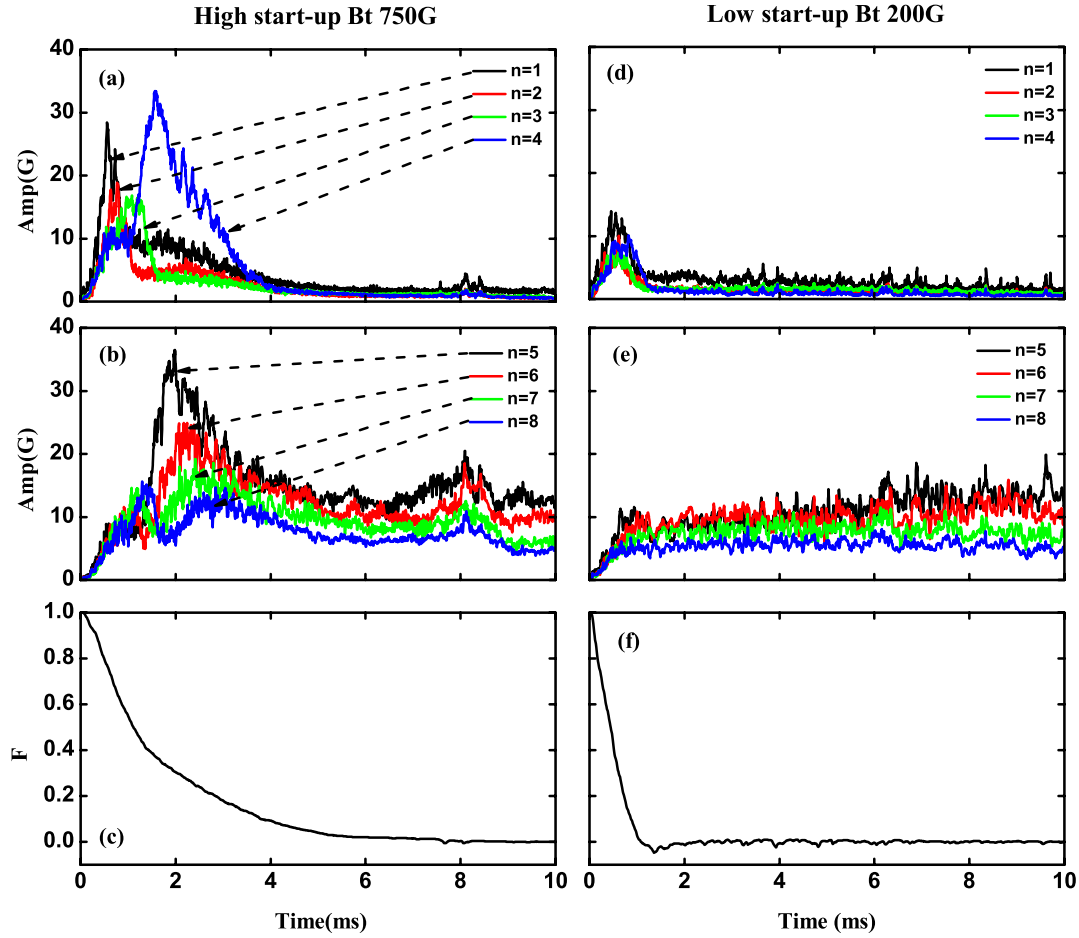


**Figure 15.** For the highest and lowest  $B_{ti}$  cases, evolution of (a) and (d)  $n = 1 - 4$ , (b) and (e)  $n = 5 - 8$ , (c) and (f) reversal parameter. Waveforms based on ensemble average of similar discharges.

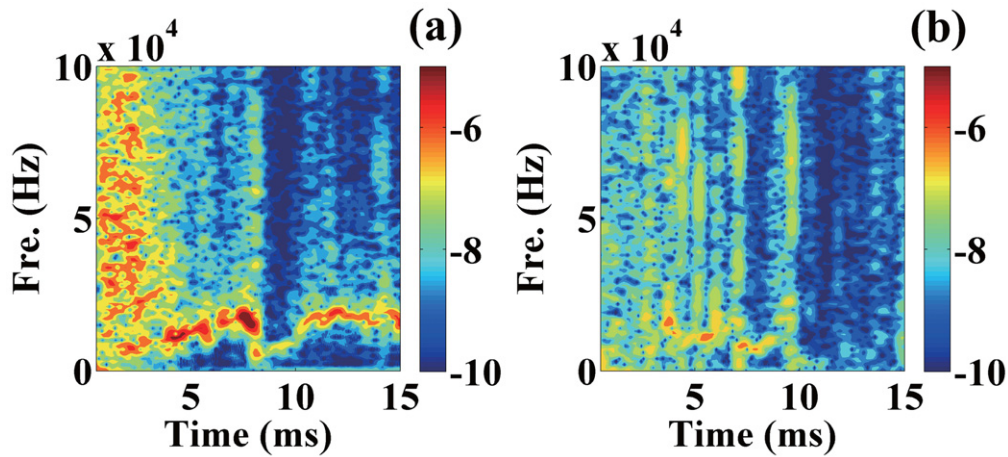


**Figure 16.** Frequency spectra of poloidal magnetic fluctuations in plasmas with the (a) highest  $B_{ti}$  (shot 1121002015), (b) lowest  $B_{ti}$  (shot 1121002097). Sample frequency 2 MHz.

frequencies  $< 10$  kHz. But the difference extends to substantially higher frequencies, as illustrated in figure 16 which contains frequency spectra from the same shots as in figure 15. In the first few ms of the discharge with high  $B_{ti}$ , the fluctuations are substantial over a broad range of frequency, extending to at least 100 kHz. The origin of these fluctuations has not been established, but given that they are

likely short-wavelength modes, they probably originate in the plasma edge, close to the sensing coils. In both spectra, discrete broadband events are also observed, corresponding to magnetic reconnection events. One also observes a low-frequency continuous band, most pronounced in the high- $B_{ti}$  case, but visible as well until about 9 ms in the low- $B_{ti}$  case. This corresponds to rotation of the modes with  $n \geq 5$ .

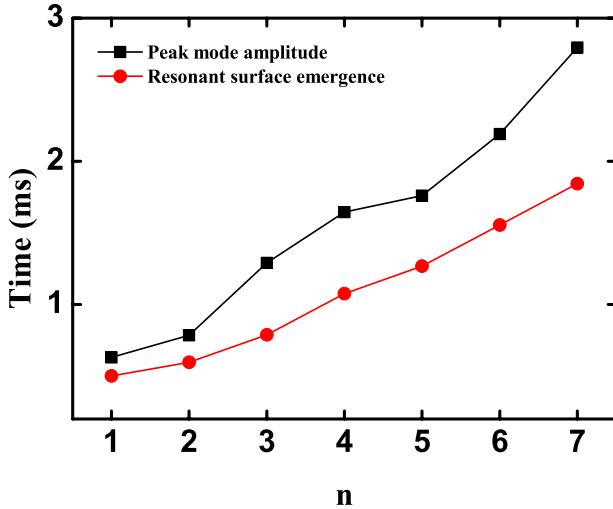


**Figure 17.** Times (red) at which each  $m = 1$  resonant surface emerges in the reconstructed equilibria and times (black) at which each of the mode amplitudes peak. For high- $B_{ti}$  shot number 1121002015.

As a check of the reconstructed evolution of the highest  $B_{ti}$   $q$  profile, we compare in figure 17 the times at which various- $n$  ( $m = 1$ ) resonant surfaces first appear in the plasma, according to the reconstructions, against the times at which each of the various- $n$  mode amplitudes peaks. As observed in the figure, the two sets of data track one another fairly well, and as expected, each resonant surface emerges in the plasma before each mode amplitude peaks.

## 5. Kinetic profiles, beta, and energy confinement

In this section we examine the evolution of the electron density and temperature, and the ion temperature, during startup with low and high  $B_{ti}$ . The electron temperature evolution is of particular importance given its contribution to the plasma resistance discussed in the following section. Profiles of the line-averaged electron density,  $n_e$ , measured with the 11-chord interferometer, are shown in figure 18. MST plasmas are fuelled via gas puffing and via recycling from the plasma-facing boundary. Multiple gas valves are distributed toroidally below the inboard midplane. The puff valves are first actuated  $\sim 20$  ms before the intended start time of each discharge. Breakdown of the neutral gas (deuterium, for the plasmas studied here) occurs with the application of the toroidal loop voltage and is aided by two thoriated-tungsten electron-emissive filaments, both located below the outboard midplane. For the two discharges in figure 18, the gas puff programming was the same, and the line-averaged density was similar between the two shots, after the time window in the figure. In both plasmas, the density quickly increases then decreases, but the initial density is larger in the high- $B_{ti}$  case. This is perhaps due to the initially more rapid rise in  $I_p$ , which may lead to more rapid ionization of the neutral gas. Another difference between these two cases, in the first  $\sim 1$  ms of the discharges, is that the line-averaged density peaks more on the inboard side with high  $B_{ti}$ . This may be linked to the  $\sim 1/R$  spatial dependence of the vacuum toroidal field profile, which

can enhance breakdown on the inboard side [20], and the fact that the field is obviously larger in the high- $B_{ti}$  case.

The evolution of the core electron temperature,  $T_e$ , profile is measured with multi-point Thomson scattering [21] every 0.5 ms. Profiles from low- and high- $B_{ti}$  shots are shown in figures 19(a) and (b). The evolution of  $T_e$  near the centre of the plasma in these two cases is shown in (c). The primary conclusion from these measurements is that  $T_e$  rises more slowly in the core with higher  $B_{ti}$ , implying that the plasma resistance is larger. That is in spite of the fact that  $I_p$ , which is responsible for heating the electrons, is initially larger with higher  $B_{ti}$ , figure 1(a). This implies that energy confinement is smaller.

We have also measured the evolution of the (majority) deuteron ion temperature,  $T_i$ . Profiles of  $T_i$  in the plasma core are shown in figure 20. These data were measured with a Rutherford scattering diagnostic, which in MST's case is comprised of a neutral helium beam scattering off of the deuterons in the plasma [22]. In contrast to  $T_e$ ,  $T_i$  initially increases more rapidly in the discharges with high  $B_{ti}$ . Furthermore, from 1–2.5 ms in the high- $B_{ti}$  discharges,  $T_i > T_e$ , comparing these temperatures at the measurement locations of Rutherford scattering. Hence, the ion heating is non-collisional and may instead be linked to the intense MHD activity described earlier. Ion heating with  $T_i$  of up to several keV occurs in MST during discrete magnetic reconnection events [23], but such heating entails the nonlinear coupling of core-resonant  $m = 1$  modes with  $m = 0$  modes, the latter all resonant where  $q = m/n = 0$  [24]. In the high- $B_{ti}$  discharges,  $q > 0$  everywhere until  $\sim 6$  ms. Modest non-collisional ion heating likely also plays a role in the low- $B_{ti}$  discharges, given the regular reconnection events noted in figure 16.

From the above kinetic profile data, we calculate the evolution of beta, the normalized plasma pressure. We also estimate the energy confinement time. For both parameters, we restrict our analysis to the highest  $B_{ti}$  discharges. This is due in part to the fact that we are interested in data where  $q(a) > 0$ , and  $q(a)$  reaches zero very quickly with low- $B_{ti}$  discharges. We utilize two definitions of beta, the total beta,

$$\beta_{\text{tot}} \equiv 2\mu_0 \left[ \frac{\int (n_e T_e + n_i T_i) dV}{\int dV} \right] / B^2(a)$$

and the poloidal beta,

$$\beta_{\text{pol}} \equiv 2\mu_0 \left[ \frac{\int (n_e T_e + n_i T_i) dV}{\int dV} \right] / B_p^2(a).$$

The total beta includes the total field at the plasma boundary. We assume an ion density,  $n_i(r) = 0.8 \times n_e(r)$ , given impurity dilution. For  $T_i$ , we include data shown above and data (not shown) measured later in time as well, and we extrapolate the radial profiles to an assumed small value of  $T_i(a)$ . The evolution of  $\beta_{\text{tot}}$  and  $\beta_{\text{pol}}$  is shown in figure 21. That both values of  $\beta$  are initially fairly large is due to the initially large plasma density, and the relatively low  $B$ . The initial difference between the two  $\beta$  values is due to the initially large  $B_t(a)$ . After 1 ms, the values of  $\beta$  are nearly identical and smaller.

The total energy confinement time is calculated using  $\tau_E \equiv W_{\text{th}} / (P_{\text{oh}} - dW_{\text{th}}/dt)$ , where all terms on the right are volume integrals. This is a more difficult quantity to calculate given the challenge in estimating the ohmic input

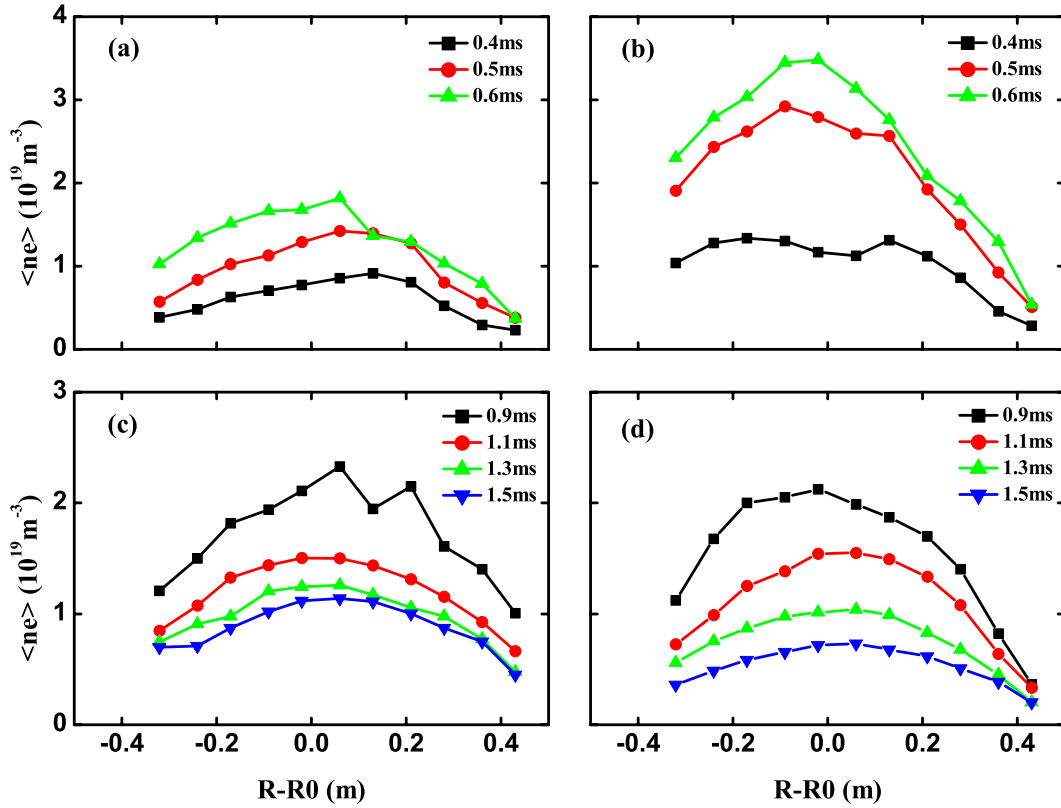


Figure 18. Evolution of line-averaged electron density at different impact parameters over the plasma diameter with (a) and (c) low  $B_{ii} = 200 \text{ G}$  (shot 1121002097) and with (b) and (d) high  $B_{ii} = 750 \text{ G}$  (shot 1121002015).

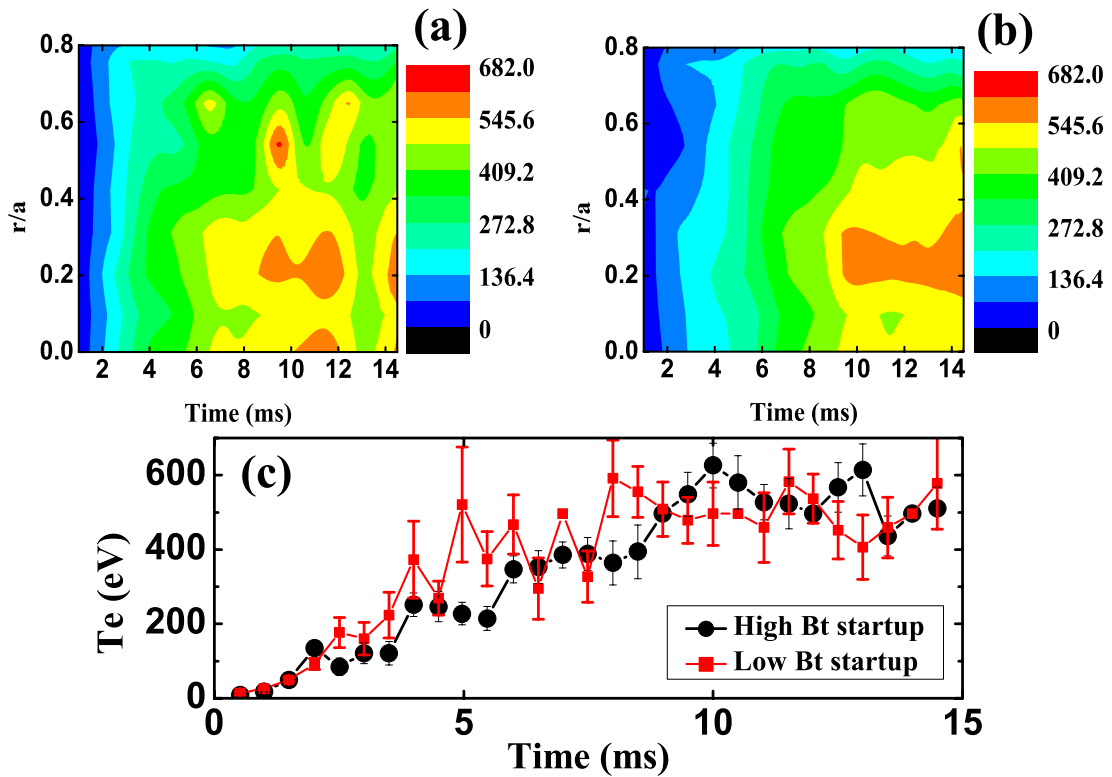
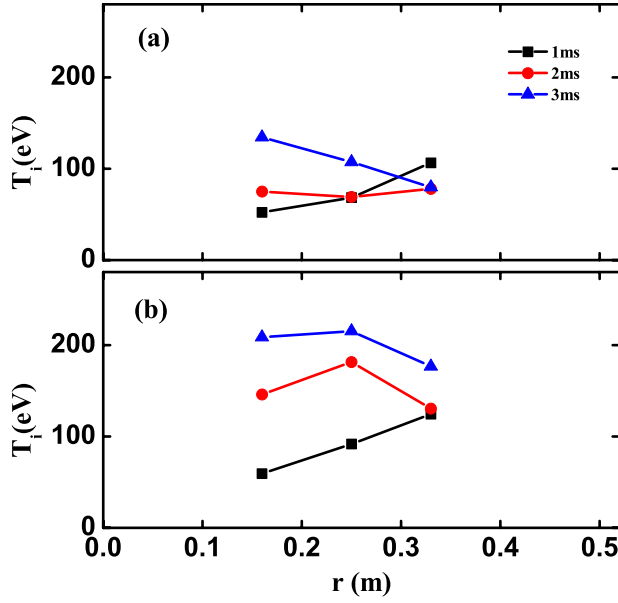
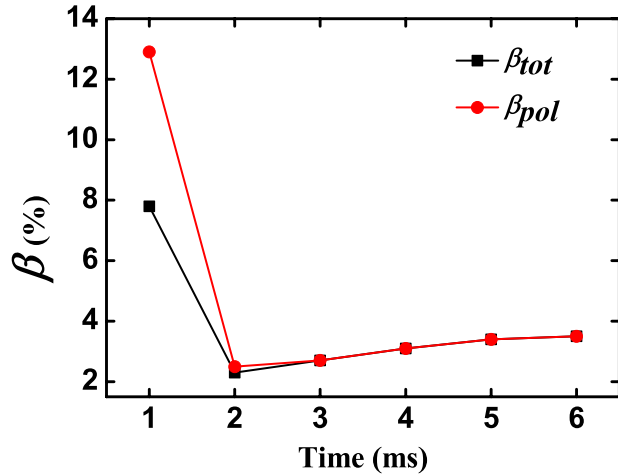


Figure 19. Evolution of electron temperature profile for (a) low  $B_{ii} = 200 \text{ G}$ , (b) high  $B_{ii} = 750 \text{ G}$  and (c) evolution of central electron temperature in both cases. Each point in (c) is based on an ensemble average of similar discharges.



**Figure 20.** Evolution of deuteron temperature profiles from a collection of plasmas with (a) low  $B_{ii} = 200$  G and (b) high  $B_{ii} = 750$  G. Data points based on an ensemble average of similar discharges. Error bars not shown for plot clarity, but error bars do not alter the conclusions drawn from these data.



**Figure 21.** Evolution of total and poloidal beta early in time in the highest  $B_{ii} = 750$  G discharge. Shot number 1121002016, one shot later than that described in previous figures, due to the availability of higher quality (but similar magnitude) Thomson scattering data.

power,  $P_{oh}$ . We estimate  $P_{oh}$  with global power balance,  $P_{oh} = P_{input} - d(W_{magnetic})/dt$ , where the input power is measured at the plasma surface, and the stored magnetic energy,  $W_{magnetic}$ , is calculated with FIRfit. From this we estimate roughly that  $P_{oh} \sim 10$  MW averaged over the first 5 ms of high- $B_{ii}$  discharges. In turn we estimate  $\tau_E \sim 0.2$  ms over the same time window. For reference,  $\tau_E \sim 1$  ms between reconnection events after startup. The confinement time during startup may be governed in part by stochastic magnetic transport, which scales as  $(b/B)^2$ . Figure 14(b) shows that  $(b/B)^2$  during startup is substantially larger than post startup, so this difference is qualitatively consistent with the difference in confinement time. Of course, the degree of stochasticity and stochastic transport depends on

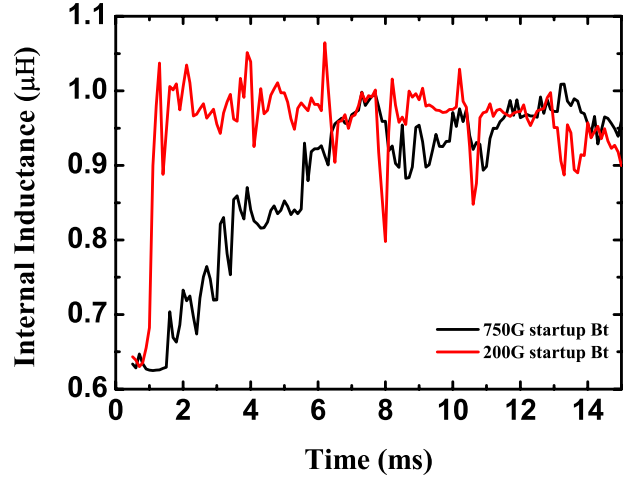


**Figure 22.** Waveforms of internal inductance for high and low  $B_{ii}$ . Shot numbers are the same as those in figure 6.

other details including magnetic shear and the width of adjacent, overlapping magnetic islands, consideration of which is beyond the scope of this paper.

## 6. Inductive and resistive consumption of flux

We now bring together the magnetic equilibrium and electron temperature data from the previous sections and apply it to understand the means by which poloidal transformer flux consumption is reduced by increasing  $B_{ii}$ . Transformer flux is expended inductively to build up the magnetic flux in the plasma, and flux is consumed resistively as the injected flux is dissipated in the plasma. The flux consumed during startup has the form  $\text{Flux}_{input} = \int_0^t L_p(t) [dI_p(t)/dt] dt + \int_0^t R_p(t) I_p(t) dt$ , where  $L_p = \mu_0 \left\{ \ln \left( \frac{8R}{a} \right) - 2 + \frac{l_i}{2} \right\}$  is the inductance of a torus,  $R_p$  is the neoclassical plasma resistance, and the integrals are with respect to time. The inductance  $L_p$  depends on the internal inductance,  $l_i = \bar{B}_p^2 / B_{pa}^2 = 2 \int_0^a B_p^2 r dr / (a^2 B_{pa}^2)$ . This reflects the shape of the toroidal current density,  $J_t$ , profile. For a perfectly flat  $J_t$  profile,  $l_i = 1/2$ , whereas  $l_i > 1/2$  ( $l_i < 1/2$ ) for a peaked (hollow)  $J_t$  profile. Note that the above expression is an approximation given that the mutual inductance between the toroidal and poloidal field circuits is not explicitly included [12, 25]. Based on measurements described earlier, we show in figure 22 the evolution of  $l_i$  with high and low  $B_{ii}$ . For the low- $B_{ii}$  discharge,  $l_i$  reaches its maximum value shortly after breakdown, but in the high- $B_{ii}$  discharge,  $l_i$  does not reach its maximum value (the same maximum as in the low- $B_{ii}$  case) until about 8 ms. This is, of course, consistent with the broader  $J_t$  profile for this high- $B_{ii}$  case in figure 8.

We compare in figure 23 the inductive flux consumption based on  $l_i$  from FIRfit with the total poloidal flux consumption shown in figure 1(d). The total flux consumption at 15 ms is, of course, smaller with high  $B_{ii}$ , and this same difference is reflected approximately in the inductive flux consumption. However, the inductive flux consumption in the high- $B_{ii}$  case is estimated to account for all of the consumed poloidal flux, and in the low- $B_{ii}$  case, the inductively consumed flux is slightly larger than the total. In both cases, the inductive flux consumption is likely overestimated modestly due to at

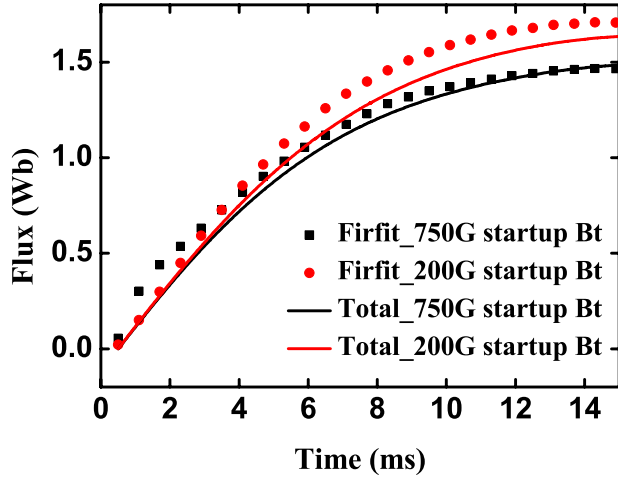


**Figure 23.** Inductive (from FIRfit) and total flux consumption for high and low  $B_i$ . Shot numbers the same as those in figure 6.

least two factors. For example, the  $J_t$  profile in the edge is not perfectly well resolved, and the assumption of zero current near the plasma edge may lead to a modest underestimate of the breadth of the  $J_t$  profile and thus a modest overestimate of the toroidal inductance and inductive flux consumption. Another factor may be finite pressure, which corresponds to finite current flowing perpendicular to  $\mathbf{B}$  ( $J_{\perp} \propto \nabla p$ ). FIRfit is not equipped to handle pressure. Hence, to gauge the approximate impact of finite pressure on the calculated inductive flux consumption, we turn to the alpha model, which is an MST adaptation of a commonly used equilibrium model for RFP plasmas [26]. The alpha model is simpler than FIRfit in that it is only constrained by external measurements of  $B_t$  and  $B_p$ . Assuming a parabolic pressure profile, for example, the alpha model was used to calculate the inductive flux consumption for different values of poloidal beta. The results are shown in figure 24 for low and high  $B_i$ . For both cases, as the pressure increases, the inductive flux consumption decreases. This is consistent with added current in the outer region of the plasma (where  $B_p > B_t$ ) broadening the toroidal current density profile and reducing the internal inductance. But even with  $\beta_{pol} = 10\%$ , considerably larger than shown in figure 21, the difference in consumed flux is  $\sim 0.1$  Wb. In addition to these two factors, the estimate of the inductive flux consumption may also be affected by the approximate nature of the flux evolution equation, described earlier.

We now turn to the resistive consumption of poloidal flux. The evolution of neoclassical resistivity profiles in the first several ms of startup in a high- $B_i$  shot are shown in figure 25. Based on Thomson scattering measurements of  $T_e(r, t)$  and an assumed  $Z_{eff}(r, t) = 2.0$ , we use MSTFit to calculate the resistivity [27]. Since  $T_e$  was already shown to be initially smaller with high  $B_i$ , for this calculation we focus on a high- $B_i$  case since it should present an approximate upper bound to the resistive flux consumption. The resistivity shown in the figure decreases rapidly with time, as expected given that  $T_e$  is increasing with time. Extending the resistivity calculation to 15 ms, we show in figure 26 the estimated resistive consumption of poloidal flux. One conclusion from this figure is that the resistive consumption of flux is much smaller than the inductive consumption. And given that

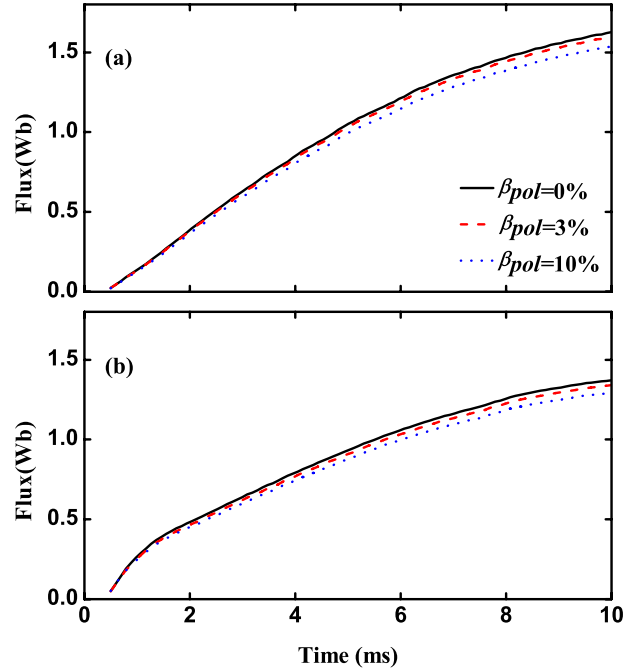


**Figure 24.** Inductive flux consumption modelled with the alpha model assuming different poloidal betas for (a) low- $B_i$  (shot 1121002097) and (b) high- $B_i$  (shot 1121002015).

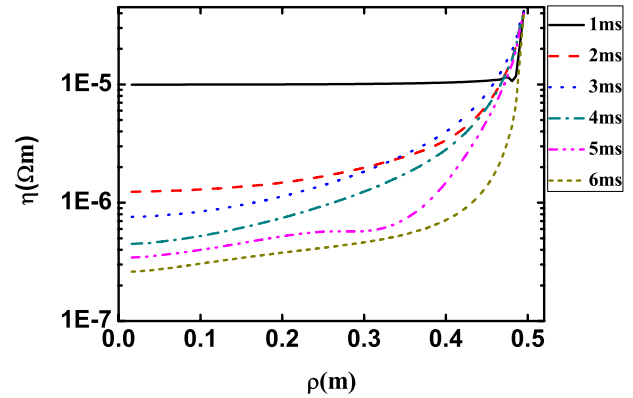


**Figure 25.** Evolution of the neoclassical resistivity in a discharge with high  $B_i$ . Analysis based on the shot occurring immediately after shot 1121002015 from figure 6 due to modestly higher quality Thomson scattering data. These are otherwise identical shots.

the resistive consumption of flux in plasmas with low  $B_i$  is probably smaller than what is shown in figure 26, we conclude that (1) the decrease in total poloidal flux consumption with larger  $B_i$  is due to the decrease in inductive flux consumption and that (2) the likely larger resistive consumption of flux in the high- $B_i$  case modestly limits the overall drop in consumed flux. One uncertainty here is in  $Z_{eff}$ , but this quantity is unlikely to be smaller than or substantially larger than 2.0. So uncertainty in  $Z_{eff}$  will not affect the overall conclusions of this work.

## 7. Summary and discussion

For the first time in a high-temperature RFP plasma, an advanced, non-invasive diagnostic set has been employed for

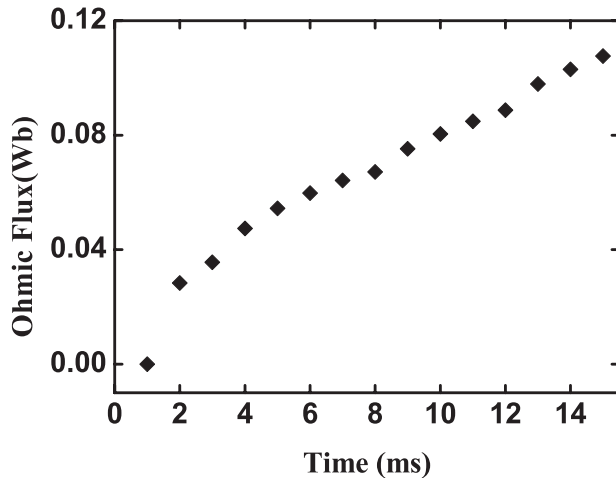


**Figure 26.** Resistive flux consumption with high  $B_{ii}$ , based in part on data shown in figure 25.

understanding the physics of plasma startup. The decrease in poloidal transformer flux consumption with larger initial toroidal field occurs due to a drop in the inductive consumption of flux. The resistive consumption of flux is estimated to be relatively small regardless of the initial toroidal field, but this consumption apparently increases with larger field due to a smaller electron temperature. The smaller electron temperature may in turn be due to the longer lasting large amplitude of magnetic fluctuations linked to the emergence of various low-order rational surfaces and a safety factor profile with a local edge minimum. Contrary to the electron temperature, the ion temperature is larger with larger initial field and reflects a non-collisional heating mechanism. This too is qualitatively consistent with the longer lasting large amplitude magnetic fluctuations.

A key question to be answered now is whether or not a further reduction of transformer flux consumption can be attained in MST. Since the resistive consumption of flux is relatively small, at least under the conditions described in this paper, it appears that the key lies in the inductive flux consumption. This implies finding means to further broaden the current density profile. One obvious approach based on the comparisons in this paper is to further increase the initial toroidal field. But from work in the ZT-40M RFP [7], startup with a larger toroidal field requires a faster ramp in the toroidal plasma current, something not yet possible in MST. But a faster ramp in the current, coupled with a finite resistive skin depth, may contribute to larger current being driven in the outer region of the plasma, thereby broadening the current profile. Simultaneously more rapid (aided) reversal of the edge toroidal magnetic field may also be critical to minimize the time to achieve toroidal field reversal and avoid an increased resistive consumption of flux. But the evolution of the current profile may also be affected directly by the strong MHD activity during startup. That is in the sense of the fluctuation-based dynamo that drives a substantial redistribution of current in RFP plasmas [28, 29]. During startup in MST with a larger toroidal magnetic field, the current profile is flatter, and this is consistent with a reduced need for the dynamo. Likewise, different equilibria will have different MHD stability properties. The local minimum in the safety factor profile is important, and this

may in part be influenced by the rate at which the edge toroidal field ramps down. These considerations imply the need for sophisticated control of the toroidal and poloidal field circuits during startup, and such control is one motivation for solid-state programmable power supplies on MST [30]. In addition to inductive control, reducing the edge plasma resistivity may also help broaden the current profile, and this is one goal of ongoing tests of boronization in MST [31].

### Acknowledgments

This material is based upon work supported by the US Department of Energy, Office of Science, Office of Fusion Energy Sciences under Award Number DE-FC02-05ER54814. This work is also supported by the Ministry of Science and Technology of China under contract No. 2011GB106000.

### References

- [1] Raman R. and Shevchenko V.F. 2014 Solenoid-free plasma start-up in spherical tokamaks *Plasma Phys. Control. Fusion* **56** 103001
- [2] Jackson G.L., Humphreys D.A., Hyatt A.W., Lohr J.M., Luce T.C. and Yu J.H. 2011 Noninductive plasma initiation and startup in the DIII-D tokamak *Nucl. Fusion* **51** 083015
- [3] Kim J. *et al* 2011 Stable plasma start-up in the KSTAR device under various discharge conditions *Nucl. Fusion* **51** 083034
- [4] Leuer J.A. *et al* 2010 Plasma startup design of fully superconducting tokamaks EAST and KSTAR with implications for ITER *IEEE Trans. Plasma Sci.* **38** 333–40
- [5] Mueller D. 2013 The physics of tokamak start-up *Phys. Plasmas* **20** 058101
- [6] Luce T., Humphreys D., Jackson G. and Solomon W. 2014 Inductive flux usage and its optimization in tokamak operation *Nucl. Fusion* **54** 093005
- [7] Phillips J.A., Baker D.A., Gribble R.F. and Munson C. 1988 Startup of reversed field pinches and current ramping using dynamo action *Nucl. Fusion* **28** 1241–54
- [8] Zanca P. and Terranova D. 2006 MHD linear stability analysis in the setting up phase of the RFX-mod experiment *Plasma Phys. Control. Fusion* **48** 407
- [9] Bodin H. and Newton A. 1980 Reversed-field-pinch research *Nucl. Fusion* **20** 1255
- [10] Collarin P., De Lorenzi A. and Piovan R. 1993 Influence of RFX engineering parameters on plasma behaviour *15th IEEE/NPSS Symp. on Fusion Engineering (Hyannis, MA)* (Piscataway, NJ: IEEE) pp 657–60 <http://ieeexplore.ieee.org/xpl/mostRecentIssue.jsp?punumber=3943>
- [11] Dexter R., Kerst D., Lovell T., Prager S. and Sprott J. 1991 The Madison Symmetric Torus *Fusion Technol.* **19** 131–9
- [12] Sprott J. 1988 Electrical circuit modeling of reversed field pinches *Phys. Fluids* **31** 2266
- [13] Brower D.L., Ding W.X., Terry S.D., Anderson J.K., Biewer T.M., Chapman B.E., Craig D., Forest C.B., Prager S.C. and Sarff J.S. 2003 Laser polarimetric measurement of equilibrium and fluctuating magnetic fields in a reversed field pinch (invited) *Rev. Sci. Instrum.* **74** 1534–40
- [14] Deng B.H., Ding W.X., Brower D.L., Almagri A.F., McCollam K.J., Ren Y., Prager S.C., Sarff J.S., Reusch J. and Anderson J.K. 2008 Internal magnetic field structure and parallel electric field profile evolution during the sawtooth cycle in MST *Plasma Phys. Control. Fusion* **50** 115013
- [15] Ko J., Den Hartog D.J., Casparly K.J., Den Hartog E.A., Pablant N.A. and Summers H.P. 2010 Two-point motional

- Stark effect diagnostic for Madison Symmetric Torus  
*Rev. Sci. Instrum.* **81** 10D702
- [16] Freidberg J.P. 1987 *Ideal Magnetohydrodynamics* (New York: Plenum)
- [17] Robinson D. 1971 High- $\beta$  diffuse pinch configurations *Plasma Phys.* **13** 439
- [18] Biewer T.M. *et al* 2003 Electron heat transport measured in a stochastic magnetic field *Phys. Rev. Lett.* **91** 045004
- [19] Reusch J.A., Anderson J.K., Den Hartog D.J., Ebrahimi F., Schnack D.D., Stephens H.D. and Forest C.B. 2011 Experimental evidence for a reduction in electron thermal diffusion due to trapped particles *Phys. Rev. Lett.* **107** 155002
- [20] Maviglia F., Albanese R., Alonso A., Lomas P.J. and JET EFDA Contributors 2011 Electromagnetic analysis of breakdown conditions in JET *Fusion Eng. Des.* **86** 675–9
- [21] Den Hartog D., Jiang N. and Lempert W. 2008 A pulse-burst laser system for a high-repetition-rate Thomson scattering diagnostics *Rev. Sci. Instrum.* **79** 10E736
- [22] Reardon J.C., Fiksel G., Forest C.B., Abdrashitov A.F., Davydenko V.I., Ivanov A.A., Korepanov S.A., Murachtin S.V. and Shulzhenko G.I. 2001 Rutherford scattering diagnostic for the Madison symmetric torus reversed-field pinch *Rev. Sci. Instrum.* **72** 598–601
- [23] Chapman B.E. *et al* 2009 Improved-confinement plasmas at high temperature and high beta in the MST RFP *Nucl. Fusion* **49** 104020
- [24] Gangadhara S., Craig D., Ennis D.A., Den Hartog D.J., Fiksel G. and Prager S.C. 2008 Ion heating during reconnection in the Madison Symmetric Torus reversed field pinch *Phys. Plasmas* **15** 056121
- [25] Schoenberg K.F., Gribble R.F. and Phillips J.A. 1982 Zero-dimensional simulations of reversed-field pinch experiments *Nucl. Fusion* **22** 1433
- [26] Antoni V., Merlin D., Ortolani S. and Paccagnella R. 1986 MHD stability analysis of force-free reversed field pinch configurations *Nucl. Fusion* **26** 1711–7
- [27] Anderson J.K., Forest C.B., Biewer T.M., Sarff J.S. and Wright J.C. 2004 Equilibrium reconstruction in the Madison Symmetric Torus reversed field pinch *Nucl. Fusion* **44** 162–71
- [28] Ortolani S. and Schnack D.D. 1993 *Magnetohydrodynamics of Plasma Relaxation* vol 156 (Singapore: World Scientific)
- [29] Antoni V., Apolloni L. and Bagatin M. 1995 Comparison of different RFX operation modes *Proc. 15th Int. Conf. on Plasma Physics and Controlled Nuclear Fusion Research (Seville, Spain)* vol 2 ([www.naweb.iaea.org/naweb/physics/FEC/STIPUB948\\_VOL2.pdf](http://www.naweb.iaea.org/naweb/physics/FEC/STIPUB948_VOL2.pdf))
- [30] Holly D.J., Chapman B.E., McCollam K.J., Morin J.C. and Thomas M.A. 2013 MST's programmable power supplies: Bt update, Bp prototype *Bull. Am. Phys. Soc.* **58** <http://meetings.aps.org/link/BAPS.2013.DPP.CP8.97>
- [31] Ko J., Den Hartog D., Goetz J., Weix P. and Limbach S. 2013 First gaseous boronization during pulsed discharge cleaning *J. Nucl. Mater.* **432** 146–51